Journal of Materials Chemistry A

ROYAL SOCIETY OF CHEMISTRY

PAPER

View Article Online
View Journal | View Issue

Cite this: J. Mater. Chem. A, 2026, 14, 17120

An *operando* spectroscopic examination of the influence of trace humidity on interdigital back contact metal halide perovskite solar cells

Mehmet E. Bayat, *[ab] Edgar R. Nandayapa, [c] Carlo Tiebe, [a] Eva L. Unger [cd] and Emil J. W. List-Kratochvil *[ef]

Controlling trace humidity is vital for both the fabrication and long-term stability of metal halide perovskite (MHP) solar cells. Relevant humidity levels are typically below 10 ppm_V, especially in glovebox-based processing and in well-encapsulated devices. Even minute amounts during fabrication can influence crystallization, introducing defects and lowering efficiency. Over time, humidity accelerates degradation of the perovskite layer and internal interfaces, ultimately reducing operational lifetime. Probing these effects at low concentrations under *operando* conditions is therefore essential for advancing device performance and durability. In this work, we employed a high-precision transfer standard dew point hygrometer to investigate humidity levels between 5 and 35 ppm_V in non-encapsulated MHP solar cells. To permit unobstructed water migration during operation, we fabricated interdigital back contact devices. *Operando* measurements revealed water transport through the perovskite layer and enabled quantification of outgassing. Under trace-humidified conditions, devices exhibited initial charge-carrier quenching, followed by gradual recovery. Notably, the photocurrent response to humidified nitrogen demonstrated that the MHP layer behaves fully reversibly within the explored timescale and across the investigated humidity levels and conditions. These findings establish a systematic *operando* framework for examining extrinsic stressors in perovskites and highlight opportunities for assessing passivation strategies.

Received 10th February 2026
Accepted 19th March 2026

DOI: 10.1039/d6ta01295g

rsc.li/materials-a

Introduction

In recent years, metal halide perovskite (MHP) materials, particularly lead-containing methylammonium (MA)/formamidinium (FA) halide perovskites, have received significant attention for their use in cost-effective and solution-processable optoelectronic devices, such as solar cells,[1–6] light-emitting diodes,[7–11] and photodetectors.[12–15] With continuous improvements, the power conversion efficiency (PCE) of MHP-based solar cells has aligned to that of silicon-based counterparts.[1] However, despite these advancements, commercially viable MHP-based solar cells remain challenging due to their still limited long-term operational stability.[4,16–18] For many applications, achieving a device lifetime of beyond 25 years – comparable to silicon-based solar cells – is required.[17,19] This highlights the necessity and importance of investigations into material, interface, and device stability under operation, considering extrinsic and intrinsic stressors.

Numerous approaches to optimize materials,[20–24] interfaces,[25–30] and device design[31–37] have been reported over time, with only a few samples discussed. For instance, studies have demonstrated that triple-cation perovskites containing caesium exhibit greater durability and enhanced phase stability.[2,20] Incorporating functionalized interlayers has been shown to effectively reduce defects in MHPs and restrain water infiltration into the MHP layer, addressing key stability challenges.[27,38] Our focus here is a different one. This work is put forward to understand the effects of stressors during the manufacture and encapsulation process. Two different types of stressors are distinguished in this context: intrinsic stressors, which include radiation, heat, and temperature (phase stability), and extrinsic stressors, which are defined by the interactions between the device/material and its gas atmosphere.[19,24,39] Regarding the atmosphere, it is well known that oxygen and humidity can affect the intrinsic MHP materials

[a]Bundesanstalt für Materialforschung und-prüfung (BAM), Richard-Willstätter-Str. 11, 12489 Berlin, Germany. E-mail: mehmet-emin.bayat@bam.de
[b]Department of Chemistry and Biology, Center of Micro- and Nanochemistry and (Bio-) Technology (Cμ), University of Siegen, Adolf-Reichwein-Str. 2, 57068 Siegen, Germany
[c]Helmholtz-Zentrum Berlin für Materialien und Energie, HySPRINT Innovation Lab, Kekulestrasse 5, 12489 Berlin, Germany
[d]Department of Chemistry, Center for the Science of Materials Berlin, Humboldt–Universität zu Berlin, Zum Großen Windkanal 2, 12489 Berlin, Germany
[e]Helmholtz-Zentrum Berlin für Materialien und Energie, Brook-Taylor-Straße 6, 12489 Berlin, Germany
[f]Department of Physics, Department of Chemistry, Center for the Science of Materials Berlin, Humboldt–Universität zu Berlin, Zum Großen Windkanal 2, 12489 Berlin, Germany. E-mail: emil.list-kratochvil@hu-berlin.de

properties.[40–42] It is reported that for oxygen interactions, the generation of superoxide through electron transfer from the photoexcited perovskite phase to molecular oxygen is causing degradation.[40,43,44] For humidity, however, there are differentiated results. It was found that an additive of small fractions of water to the perovskite precursor solution or a humidified atmosphere during annealing results in an increased PCE, as the water/humidity enhances the crystallization of the perovskite thin film and its surface coverage.[45–48] In addition, it was revealed that trace humidity exposure enhances the n-type surface character and reduces the work function of a MHP-based thin film.[40] On the other hand, there are many groups that postulate a water-induced (humidity-induced) degradation mechanism and the formation of non-perovskite phases.[49–52] The proton affinity of the perovskite is often highlighted in this context.[51,53]

However, these studies concentrate on high humidity volume fractions, although ideally, well-encapsulated solar cells should not experience such high amounts of humidity. The relevant humidity thresholds for these types of studies should be well below 30 ppm_V (parts per million per volume) and below 10 ppm_V for optimal glovebox-controlled scenarios. The threshold values are determined by the quality standard for technical gases of grade 5.0 (99.999% purity), which specifies to contain no more than 10 ppm of characterized impurities (*e.g.*: N_2, O_2, H_2O, CO, CO_2).[54] However, based on experience with our glove-boxes, trace humidity readings of 2 ppm_V to peak readings of 30 ppm_V (at high laboratory utilization) could be quantified using a traceable measuring device. To the best of our knowledge, there are only very few publications concerning this trace humidity range.[40,55]

Interdigital back contact (IBC) solar cells based on MHPs aim to further simplify the fabrication process by placing both the anode and cathode for charge collection on the rear side, improving light absorption, and eliminating the need for a front electrode.[56] Nevertheless, the PCE of MHP-based IBC solar cells is well below expectations and not competitive against sandwich-type MHP-based solar cells, as the charge carrier extraction is limited due to the longer diffusion lengths.[56–60] Based on this, various alternative back contact (BC) architectures have been explored. These investigations were significantly advanced by the introduction of designs such as quasi-IBC solar cells and honeycomb quasi-interdigitated electrode solar cells.[61–63] However, the highest stabilized PCE reported with these BC architectures is 8.6%, which does not yet justify the costly and sophisticated lithographic fabrication of BC electrode structures.[63,64]

Independent of device and design optimization, we employ unencapsulated IBC solar cells here to allow unimpeded water migration into the MHP layer and device during operation. For the fabrication of the IBC solar cell, we have adopted a fabrication protocol published recently by Alsari *et al.*, which allows for making IBC solar cells without the extensive use of lithographic equipment.[57,58]

In a prior publication, we demonstrated that trace humidity has a reversible quenching effect on the photoluminescence (PL) emission of a MHP-based thin film.[55] We identified the nature of the water-induced PL-quenching process and described the underlying diffusion kinetics. In this study, we expand upon this finding by showing that the photocurrent of an unencapsulated MHP-based IBC solar cell is similarly affected in a trace-humidified nitrogen atmosphere, *in operando*. Trace-humidity volume fraction measurements were performed continuously, with full traceability to national metrological standards. Water migration within the IBC solar cells, carefully fabricated in a controlled, dry environment, was observed in operation, as evidenced by trace humidity emissions that were precisely quantified. Utilizing a highly precise and accurate measurement setup, coupled with a two-site Stern–Volmer analysis, we were able to define a trace-humidity guideline value critical for preserving the intrinsic properties of the MHP during fabrication and encapsulation.

Experimental section

Substrate preparation

Interdigitated pre-patterned ITO substrates with a consistent gap of 50 μm were purchased from Ossila Ltd (product number: S161). Prior use, the substrates were successively cleaned in acetone, isopropanol, ethanol, and distilled water for 10 minutes in a sonic bath and then dried with clean nitrogen.

Electrically conductive adhesive (Conrad Electronic SE, Kemo L100, product number: 1387067-62) was applied to the contact points of a channel side with a brush, where the selective layer was to be deposited, as shown in the SI. After the conductive adhesive was fully hardened and dried, electrical connection legs (Ossila Ldt, product number: E242-roll) were attached to the corresponding contact side. The connection legs were bent as shown in Fig. S1b.

TiO_2 deposition

The titanium dioxide layer, which was deposited first, was obtained through cathodic electrochemical deposition. Titanyl sulphate (64.0 mg, 0.040 mmol; Sigma-Aldrich, product number: 14023-100G) and 30 vol% hydrogen peroxide (366 μL, 0.047 mmol; Sigma-Aldrich, product number: H1009-100ML) were transferred into a small glass vial filled with 20 mL of distilled water. The reaction mixture was mixed using a vortex mixer for 2 minutes at 2500 rpm and then placed in a sonic bath for 1 minute. The prepared cloudy yellow-orange solution was stored in the fridge for 5 minutes. The solution was repeatedly mixed and stored in the fridge until a clear peroxo-titanium stock solution (0.002 mmol mL^{-1}) was obtained, shown in Fig. S2a. The peroxo-titanium stock solution had to be freshly prepared each time and be used quickly.

1 mL of the peroxo-titanium stock solution was transferred into 25 mL of an aqueous 0.1 M potassium nitrate solution (Sigma-Aldrich, product number: 31263-500g). The obtained yellow reaction solution (0.08 μmol mL^{-1}) served as deposition bath for the cathodic electrochemical deposition and was prepared afresh for each substrate.

The electrochemical deposition was performed using a Keithley potentiostat 2450-EC. A three-electrode setup was

used, with a platinum mesh as the counter electrode and a platinum wire as the pseudo-reference electrode. A crocodile clip was attached to the bent connecting leg on the prepared substrate. This served as the working electrode. The chronoamperometry method was used for the deposition process, with a potential of −2.20 V applied for 10 seconds. The reaction solution was not stirred during the deposition. A brown layer formed on the ITO fingers (Fig. S2b). The conductive adhesive was carefully removed using a cotton swab soaked in isopropanol and rinsed multiple times in water, ethanol, and isopropanol.

Further, the treated substrate was annealed in ambient atmosphere. First, it was dried at 150 °C for 15 minutes on a clean hotplate (IKA C-MAG HS 7 digital). Subsequently, the temperature of the hot plate was increased to 500 °C for 60 minutes. During the annealing procedure the formation of anatase titanium dioxide is indicated by a colour change of the deposited layer to a pale yellow. Once the substrate reached ambient temperature, an ozone treatment was applied for 5 minutes. Afterwards, it was rinsed in deionized water, ethanol, and isopropanol. Finally, the substrate was annealed a second time at 500 °C for 20 minutes and cooled down to room temperature on the hot plate (Fig. S2c).

Poly(3,4-ethylenedioxythiophene) deposition

The poly(3,4-ethylenedioxythiophene) (PEDOT) layer was deposited by electrochemical polymerization. On the titanium dioxide-coated substrate, conductive adhesive was applied on the contact points to be coated with PEDOT, and a connecting leg was attached as described above (Fig. S3a).

The reaction solution was prepared by dissolving lithium perchlorate (2.12 g, 0.02 mol; Tokyo Chemical Industry Company Limited, product number: L0379) in 20 mL of propylene carbonate (Thermo Fisher Scientific, product number: 131560010) by alternating ultrasonic treating and mixing using a vortex mixer. 3,4-Ethylenedioxythiophene (21.4 μL, 0.20 mmol; Thermo Fisher Scientific, product number: H56533.06) was then dissolved in the propylene carbonate solution and mixed using a vortex mixer. The resulting solution (10 μmol mL^{-1}) served as deposition bath for the electrochemical polymerization and was used for up to 10 substrates.

A three-electrode setup was applied, consisting of a platinum mesh as the counter electrode, a silver wire as the pseudo-reference electrode, and the substrate as working electrode. The deposition was carried out using the chronoamperometry method with a deposition time of 10 seconds and an applied potential of +1.25 V. During the deposition, it was important to ensure that the conductive adhesive was not in contact with the reaction mixture, as it would have dissolved in it. The deposition bath remained unstirred throughout the process. After deposition, the substrate was soaked in distilled water for 5 minutes. The conductive adhesive was then carefully removed using a cotton swab soaked with isopropanol. Subsequently, the substrate was rinsed several times, alternating between distilled water and isopropanol, until no visible impurities were present. The substrate underwent a final cleaning process by rinsing alternately in ethanol and distilled water for three cycles and was dried with clean nitrogen (Fig. S3b).

Perovskite thin film deposition

The substrate with PEDOT and titanium dioxide layer was carefully taped using crepe tape, as shown in Fig. S4a. The taped substrate was then transferred into the sluice of a glove box and vacuum dried for 15 minutes under several nitrogen flushes.

The MHP precursor solution was prepared as described in ref. 2. Lead iodide (product number: L0279) and lead bromide (product number: L0288) were purchased from Tokyo Chemical Industry Company Limited. Formamidinium iodide (product number: DN-P10-4N) and methylammonium bromide (product number: DN-P09-4N) were obtained from Dyenamo AB. Caesium iodide was purchased from Abcr GmbH (product number: AB109298). Anhydrous dimethylformamide (product number: 276855-250ML) and dimethyl sulfoxide (product number: 227056-250ML) were purchased from Sigma-Aldrich. 50 μL of the precursor solution was deposited and evenly spread onto the interdigitated area of the substrate. All samples were spin-coated at 3000 rpm for 35 seconds with an acceleration time of 5 seconds. 250 μL of anhydrous toluene (Sigma-Aldrich, product number: 244511-100ML), was used as anti-solvent after 25 seconds of the starting process. Note that anisole and ethyl acetate were also tested, but toluene yielded the highest thin-film quality. Annealing was conducted at 100 °C for 45 minutes. Once the device had cooled down, the used crepe tape was carefully removed with care to avoid adhesive residue. If the device was not to be measured on the same day, it was vacuum sealed and stored in the dark in a nitrogen filled glove box.

Current–voltage measurements

Current–voltage (*J*–*V*) sweeps were conducted with a Keithley 2450 source measuring unit in 0.05 V steps. At each voltage step, the bias was held constant for 0.2 seconds before measuring the current. An active area of 0.260 cm^2 was used for the calculation of *J*–*V* parameters. Measurements at maximum power point (MPP) in trace humidity experiments were performed with a Brennstuhl EL 2050 M lamp. Otherwise, a Sciencetech SciSun-300 solar simulator under 1 sun radiance at AM1.5G standard was used. The power output to the IBC device was equal for both lamps (see SI). An in-house designed sample holder was used for trace humidity measurements (see SI). Otherwise, a push-fit test board for 20 × 15 mm substrates (Ossila Ltd, product number: P2008A1) was used to provide electrical connection.

Trace humidity generation and quantification

Trace humidified nitrogen was continuously generated by applying dynamic dilution using an in-house developed gas mixing system equipped with Bronkhorst EL FLOW Prestige thermal bypass mass flow controllers (MFC). The nitrogen used was purchased from Linde GmbH in a quality grade of 5.0 (99.999% purity). Trace humidity quantification was conducted after the measuring cell with the transfer standard dew point hygrometer MBW 373LX (Ser. No.: 19 0416), which has a valid

accredited calibration according to ISO/IEC 17025 (Cert. No.: 7122MBW2019). Readings of the dew point hygrometer were generated every 10 seconds with the software Gecko R2. The measured frost point temperatures were derived to the water vapor partial pressure using the ITS-90 Sonntag equation.[65] Trace humidity concentrations were calculated according to ISO 14912:2025 using a truncated, linear virial equation (second-virial-coefficient approximation).[66] Additional information on the virial coefficients of water vapour is summarized in ref. 67.

Temperature measurements

Surface temperature measurement of the measuring cell was conducted by applying PT1000 surface sensors, purchased from otom Group GmbH. Readings were recorded using a Fluke Calibration 2638A digital multimeter.

Results and discussion

Experimental setup

A simplified pipe and instrumentation diagram (P&ID) of the experimental setup is depicted in Fig. 1. Grade 5.0 nitrogen was fed into a molecular sieve trap at 5.0 bar(a) to reduce the trace humidity blank value from ≤5 ppm_V to approximately 1 ppm_V before entering the gas mixing system. In the gas mixing system, dynamic dilution is applied: a continuous dry partial gas flow is combined with a continuous humid partial gas flow to generate a defined trace-humidified nitrogen output. The humid partial gas flow is generated using the saturation method.[68] Further details on the humidification unit can be found in the supplement of ref. 69. The trace-humidified nitrogen is then fed into a measuring cell, consisting of a CF cube equipped with a sample holder for the IBC solar cell and a borosilicate viewport to permit light transmission into the measuring cell (see SI). The measuring cell and lamp were placed in a temperature chamber to ensure a constant environmental temperature. Measurements were conducted at approximately 1 sun with illumination on the front side of the IBC solar cells. The sample holder of the IBC solar cell was electrically connected to a source measure unit. The gas output of the measuring cell was connected to the transfer standard dew point hygrometer to quantify continuously the trace-humidity volume fractions *in operando* and *in situ*. The gas flow through the measuring cell was 2700 mL_n min^{-1}, with approximately 1700 mL_n min^{-1} being fed into the dew point hygrometer (mL_n min^{-1} = flow unit at standard conditions of 0 °C and 1013.25 mbar(a)). Further details on the experimental setup and dynamically generated trace-humidity sample gases are provided in the SI.

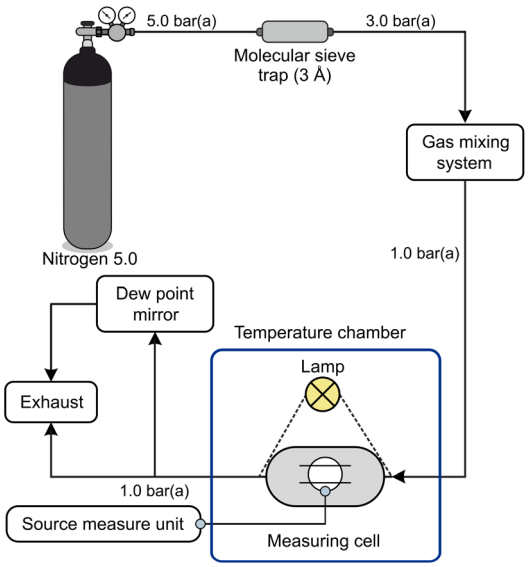

Fig. 1 Schematic representation of the P&ID of the experimental setup. Clean, dry nitrogen was fed into a gas mixing system that enabled trace humidification. The trace-humidified gas was subsequently fed into the measurement cell, which housed the IBC solar cell and was maintained under constant illumination. Therefore, dynamically generated sample gases were applied to quantify humidity-induced effects.

Interdigital back contact solar cells – fabrication and basic characterization

Fig. 2a presents a schematic sketch of the IBC solar cell fabricated following a recipe described in literature.[57,58] An interdigitated, pre-patterned indium tin oxide (ITO) glass substrate was used, on which selective electron and hole contacts were electrochemically deposited. Here, titanium dioxide was cathodically deposited to serve as the electron-selective contact (depicted in red), while PEDOT was deposited *via* electrochemical polymerization on the opposite ITO finger to function as the hole-selective contact (depicted in blue). The selective interdigitated electrodes (50 μm spacing and 100 μm width) were coated with an average thickness of (66 ± 14) nm titanium dioxide and an average thickness of (37 ± 8) nm PEDOT (see SI). The MHP layer, consisting of $Cs_{0.05}(MA_{0.17}FA_{0.83})_{0.95}Pb(I_{0.83}Br_{0.17})_3$, was spin-coated onto the interdigitated electrode area, represented in brown, with an average thickness of (237 ± 45) nm (see SI). The total active area of the device was 0.260 cm^2 (5 × 0.052 cm^2). Further, a detailed topographical characterization of the device and of each fabrication step is provided in the SI. In Fig. 2b a picture of an IBC solar cell is presented (after trace humidity measurements), and Fig. 2c shows typical *J–V* measurements of an IBC solar cell. In the first sweep after fabrication, a linear *J–V* characteristic is observed, while both short-circuit current (J_{SC}) and open-circuit voltage (V_{OC}) are very low. The performance of the IBC solar cells gradually improves with the number of conducted *J–V* sweeps. For this specific device, after 70 sweeps a maximum J_{SC} of 0.05 mA cm^{-2} and V_{OC} of 0.53 V was achieved. Please note that we made very similar observations for all working devices, regardless of sweeping the device in forward or reverse bias direction, as depicted in the SI. All observations are also consistent with earlier literature reports of similar IBC solar cells.[57] Based on these observations all tested cells have been preconditioned with this *J–V* procedure. For all working cells we observed PCEs of around 10^{-3}%.

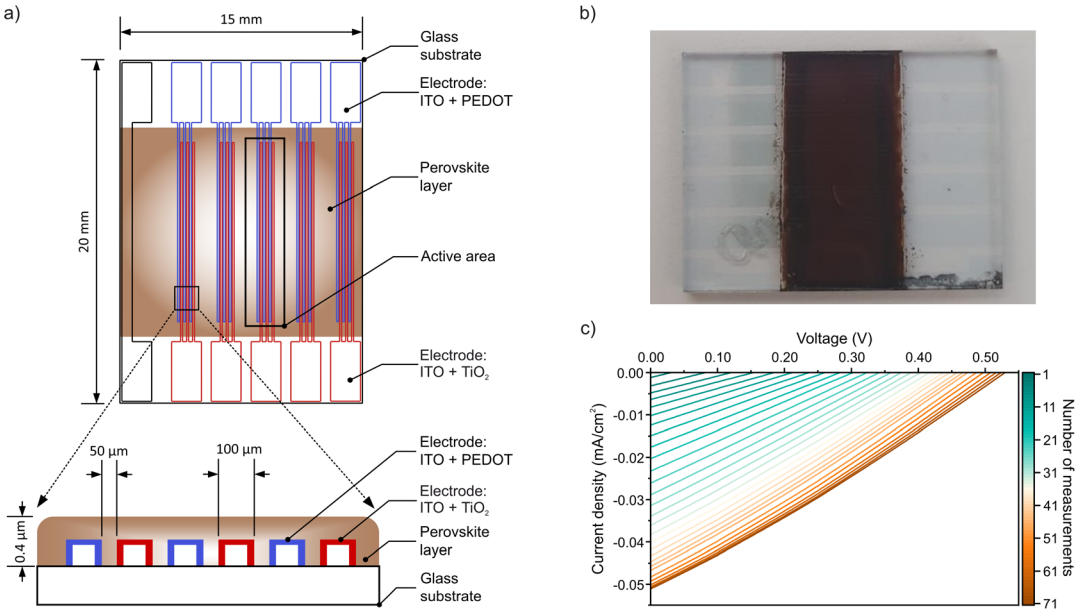

Fig. 2 (a) Schematic sketch of the structure and dimensions of the IBC solar cells. Above as top view and below a cross-section through the interdigital interface. (b) Top view of a manufactured IBC solar cell (after trace-humidity measurements). (c) Several *J*–*V* characteristics of an IBC solar cell measured in sequence. The characteristics gradually improved with the number of conducted *J*–*V* sweeps.

Even though the solar cells demonstrate very low photocurrent with good photovoltage, the photocurrent is in a range in which reliable measurements with very low uncertainties are possible. Moreover, after preconditioning, all devices showed good stability and moderate degradation during the performed measurements, as discussed below.

Water outgassing

During *J*–*V* pretreatments and under constant illumination, traces of water emerged from the solar cell in the form of trace humidity over a period of 80 minutes (see Fig. S17). Interestingly, literature indicates that water outgassing is observed only at temperatures around 60 °C for MHP thin films.[70] Our observations show that water outgassing started with the beginning of the *J*–*V* pretreatment, although the IBC solar cell was already continuously illuminated (for two hours) and surrounded by a clean, dry nitrogen environment (less than 1.8 ppm_V trace humidity, decreasing). It is important to note that great care was taken in the manufacture of the IBC solar cells to avoid traces of water. For instance, the substrate with deposited selective layers was vacuum dried for 15 minutes under several nitrogen flushes before being transferred into the glovebox. In addition, the IBC cell was annealed in clean dry nitrogen at 100 °C for 45 minutes. Thus, to the best of our knowledge, these cells have been manufactured and tested under controlled, inert, and dry conditions on a laboratory scale. Therefore, outgassing of water suggests that local temperatures of 60 °C or higher occurred within the active areas of the MHP layer during device operation. It should be noted that the analytical method used for quantifying water outgassing at this trace level was highly specific and free of interference from potentially outgassing MHP degradation products, as explained in detail in the SI. As a result, the emission of water from the depicted IBC solar cell at the onset of *J*–*V* pretreatments was quantified with approximately 8.7 µg (calculation presented in the SI), showing that the source of emission is not related to water monolayers adsorbed on the MHP surface. Further, the temperature increase within the material was attributed to heat generation from Joule heating, which may facilitate the diffusion of water molecules trapped in the MHP crystal lattices, interfaces, or electrodes.

Considering that water emission occurs only in the active areas, two hypotheses can be concluded. First, the outgassing process from the MHP layer is not limited to the active area, suggesting a migration of water into the active areas. This migration is likely driven by a moisture gradient within the MHP layer, which is induced by the water emission at the active areas. The deposited mass of MHP on the active areas was determined to be approximately 26 µg (see Section S4.1). Consequently, it is improbable that about 30% of the MHP mass at the active areas would have consisted of water, especially given that it underwent annealing. Second, moisture trapped within the ITO/PEDOT/TiO_2 or at their interfaces in the active areas migrates out of the system and through the perovskite layer. Due to the long diffusion time, we tend to assume a dominant contribution of the first hypothesis. However, regardless of the interpretation, trapped water, irrespective of its origin, migrates through the perovskite layer and is removed from the system.

If this observation is applied to classic perovskite solar cells, the migration of water through the whole device could trigger corrosion processes at metal electrodes or water-sensitive interfaces, as described in the literature.[52,71–73] Additionally, water can act as a catalyst, reducing the formation energy of

halide defects, the activation energy for halide ion migration, and the potential barriers for phase transformation.[74–76] Consequently, the experimentally observed outgassing of water suggest that trapped water most likely migrates through the device and alters intrinsic properties of the MHP, such as its phase stability.

Reversible response behaviour of the photocurrent

Fig. 3 shows a time series of a conducted measurement with a $Cs_{0.05}(MA_{0.17}FA_{0.83})_{0.95}Pb(I_{0.83}Br_{0.17})_3$ IBC solar cell in trace-humidified nitrogen. This MHP composition was selected because Cs-containing triple-cation perovskites have been reported to exhibit enhanced thermal stability, suppressed phase impurity formation, and improved tolerance to processing variations compared with simpler MA- or FA-based formulations.[20] Accordingly, this composition represents a stable and well-established benchmark absorber for the present study. In layer 5 and 4, the time series shows a stepwise increase in amounts of trace humidity generated by the gas mixing system, measured as frost point temperatures (condensation temperature) and volume fractions in ppm_V, rising from a low of approximately 5 ppm_V (around −65.5 °C) to a peak of around 34 ppm_V (around −51.3 °C). Subsequently, the trace humidity volume fractions are shown to decrease stepwise, returning from the peak value back down to around 5 ppm_V. All trace humidity sample gases are characterized as frost point temperatures, volume fractions, and concentrations in the SI (see Table S1). Between each trace humidity level, a drying phase was conducted, allowing the MHP to regain its properties. Each humidification phase was conducted over a period of 90 minutes, while the subsequent drying phase lasted 180 minutes, resulting in a total experimental duration exceeding 2.5 days. The temperature at the outer surface of the measuring cell is presented in layer 3, where a stable thermal environment with slightly varying temperatures around 21 °C was observed. Layers 2 and 1 present the current density of the IBC solar cell in trace humidified conditions. The current density was measured with a constant applied voltage of 0.35 V at the MPP (V_{OC} of 0.73 V for the depicted IBC solar cell). Due to the global non-linear degradation behaviour, a single non-linear baseline function was fitted to the entire data set. The baseline was determined using data points recorded sufficiently before and after the trace humidity injection as anchor points and subsequently subtracted from the raw current density data shown in layer 1 (further details on the baseline methodology are provided in the SI). Consequently, a positive baseline-corrected current density in layer 2 corresponds to a deterioration in device performance, arising from a shift of the raw current density toward less negative values. However, it was observed that each trace humidity phase led to a significant charge-carrier quenching. Remarkably, while the trace-humidified nitrogen was still flowing through the measuring cell, it was observed that the current density recovers and slowly increases over time again. Switching back from humidified nitrogen to dry nitrogen, a further restoration of the current density to baseline level was observed.

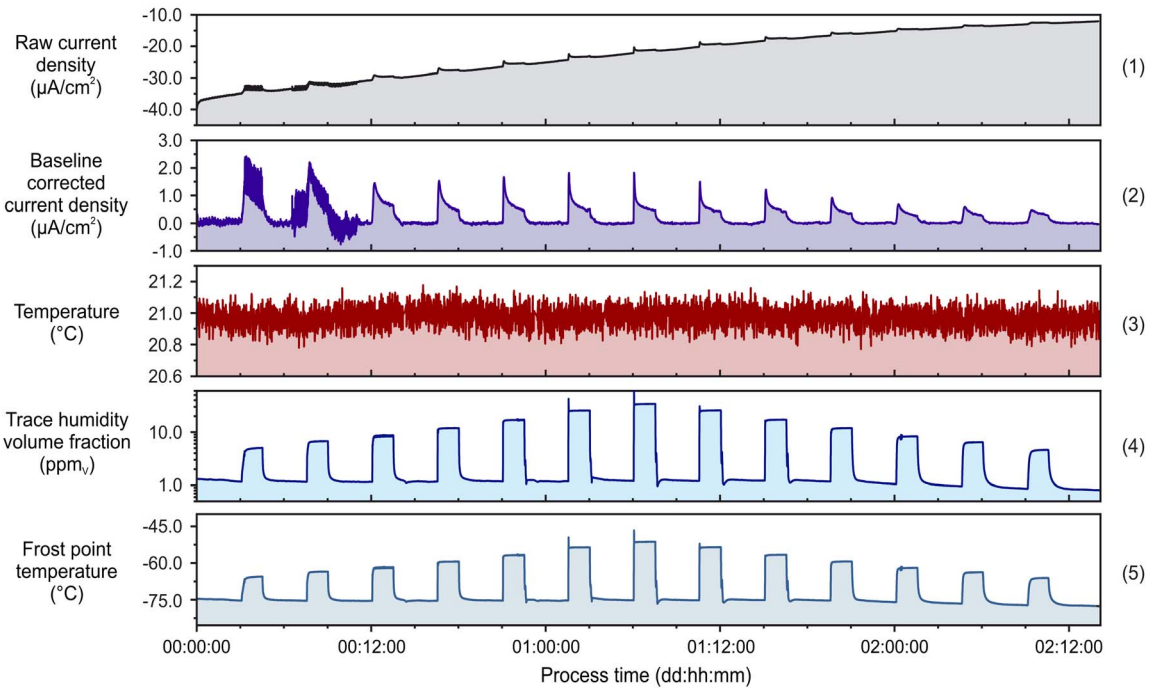

Fig. 3 Time series of increasing and decreasing amounts of trace humidity investigated at MPP with a constant applied voltage of 0.35 V. Layer (1) depicts the raw measured current density while layer (2) presents the baseline-corrected current density. Layer (3) illustrates the temperature directly measured on the measuring cell. Layer (4) demonstrates the trace humidity volume fraction in ppm_V, derived from the measured frost point temperature (direct proportional to the water vapor partial pressure) and the pipe pressure at the mirror. Layer (5) presents the condensation temperatures, expressed as frost point temperatures (condensation as ice), determined with a reference dew point hygrometer.

Additionally, readings of the current density for the first two trace-humidified phases showed a significant noise of unknown origin. Importantly, this noise was already present under dry conditions and did not correlate with the humidity-induced response. Comparable noise was not observed when using a fully shielded commercial IBC sample holder (push-fit test board). However, this holder could not be integrated into the trace humidity setup due to geometric constraints. These observations indicate that the noise does not originate from the device, the MHP material, or from humidity-induced interactions. The source of the noise could not be assigned unambiguously, as it appeared randomly and could not be correlated with any specific measurement parameter or laboratory event, suggesting that it was likely caused by external influences affecting the experimental setup.

In Fig. 4a, the current density readings for each humidified phase, extracted from the data set of Fig. 3 with pre- and post-conditioning periods, are presented as stacked, baseline-corrected data sets. Generally, a baseline correction was necessary due to the degradation behaviour occurring immediately after reaching a maximum optoelectronic power output after the conducted *J*–*V* pretreatments (see SI). It is evident that at the beginning of the experiment and under dry nitrogen conditions, prior to any humidification, a pronounced global degradation mechanism is already observable. Furthermore, within the investigated trace humidity volume fractions that followed a pyramid-shaped measurement program, no acceleration of degradation is observed. Instead, the degradation rate progressively flattens over time.

Consequently, degradation effects were always observed in long-term measurements, even with control samples in dry nitrogen without humidification (see SI). This behaviour strongly suggests that the primary cause of degradation is light- and heat-induced, leading to the decomposition of the organic cations FA^+ and MA^+, well documented in the literature.[70,77–80] For example, the reduction of methylammonium by free electrons

$$2CH_3NH_3^+ + 2e^- \rightarrow 2CH_3NH_2\uparrow + H_2\uparrow \quad (1)$$

or the heat-induced dissociation of $MAPbI_3$

$$MAPbI_3 \xrightarrow{\Delta T} PbI_2 + CH_3NH_2\uparrow + HI\uparrow \quad (2)$$

show very clearly the formation of gaseous products.[70,80] However, we did not observe that the MHP layer turned yellow after the measurements, as exemplary shown in Fig. 2b. This leads us to conclude, in agreement with the literature, that PbI_2 decomposes into Pb and I_2 under long-term white light illumination (as performed here), resulting in the formation of metallic Pb^0.[81] The unencapsulated and unembedded nature of the IBC device, combined with a continuous flow of clean nitrogen, likely accelerated the light- and heat-induced degradation, as gaseous reaction products were continuously removed from the system, thereby shifting any existing chemical equilibrium reactions towards the degradation products.

Although a global degradation trend is present in the long-term measurements, it does not compromise the comparability of the humidity-induced effects. The humidity-related changes in current density are evaluated relative to a global non-linear baseline. This approach explicitly separates humidity-induced effects from long-term degradation. Consequently, the extracted signals reflect raw responses to trace humidity rather than degradation artifacts. It is important to note that all subsequent data analyses refer always to baseline-

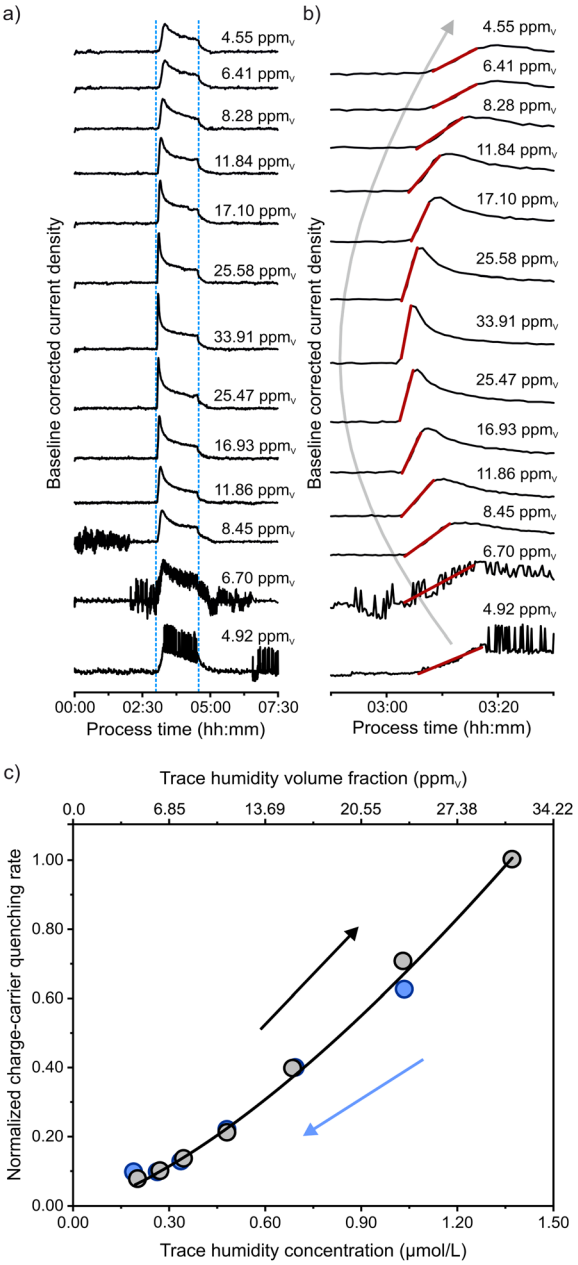

Fig. 4 Visualization of the response behaviour to trace-humidified nitrogen. (a) Stacked baseline-corrected current density with pre- and post-period in dry nitrogen. The trace-humidified phase is illustrated in blue. (b) Magnification of the trace humidity phase with linear fits in red. (c) Correlation of the determined charge-carrier quenching rate in normalized form (slope of the linear fit) with the investigated trace-humidity concentrations/volume fractions for increasing (in black) and decreasing (in blue) amounts. The fit of the pseudo-rate equation is presented in black.

corrected signals and therefore explicitly represent humidity-induced effects.

Continuing, our previously published experimental results on MHP-based thin films under varying trace-humidified argon conditions showed that the PL emission recovered to its baseline level on a timescale of about 5 minutes.[55] In contrast, at a timescale of 90 minutes, the recovered current density in trace-humidified nitrogen still shows a trend towards regeneration. This indicates that the MHP has not yet reached an equilibrium state in the humidified conditions. However, preliminary measurements under trace-humidified nitrogen conditions showed that recovery to the baseline level does occur within 90 minutes of humidification. Therefore, the time for a complete recovery from the trace humidity interaction of the current density seems to be device-dependent, probably related to the crystallinity and grain size of the MHP layer.

The response behaviour to the investigated trace humidity sample gases demonstrates high sensitivity, as evidenced by the sharp transition in current density that occurs when switching from dry to trace-humidified nitrogen. To better describe the response behaviour, the transition in current density – from the point of trace humidity injection into the system to the point of maximum charge-carrier quenching – was fitted linearly, as shown in Fig. 4b. The slopes of the linear fits were observed to rise with increasing trace-humidity volume fractions and fall back in a similar manner as the volume fractions decreased. This is particularly evident when the slopes are correlated with the investigated trace humidity concentrations/volume fractions, as shown in normalized form in Fig. 4c. Here, the obtained slopes are interpreted as charge-carrier quenching rates. It is evident that the rates for increasing trace humidity levels (black) match those for decreasing trace humidity levels (blue). These results show that, although degradation is present, the current–density response and sensitivity of the MHP-based IBC solar cell to trace-humidified nitrogen are fully reversible within the explored timescale and conditions, providing independent evidence that the degradation process does not affect the charge-carrier kinetics (in this study).

To gain deeper insight into the charge-carrier quenching rates, a pseudo-reaction-rate approach was adopted.[69] With this simplified model, the interaction of water vapor with the MHP-based material is described by assuming an effective adsorption or accommodation of water at quenching-relevant surface sites, schematically represented by eqn (3):

$$\text{MHP-site} + H_2O_{(g)} \rightarrow \text{MHP–}H_2O_{(ad)} \quad (3)$$

Accordingly, MHP-sites interacting with water are assumed to be initially inactive with respect to charge-carrier participation, thereby reducing the effective charge carrier population that contributes to current density. Further microscopic processes like defect-mediated interactions, surface diffusion or recrystallization cannot be resolved individually within the measurements.

However, based on this simplified assumption, the pseudo-rate expression can be written in logarithmic form as

$$\ln(r) = \ln(k') + m \times \ln([H_2O_{(g)}]) \quad (4)$$

which is shown as the black fit in Fig. 4c. For clarity, the pseudo-rate relationship is displayed in linear rather than logarithmic scaling. In this expression, r denotes the charge-carrier quenching rates, while the slope m corresponds to the apparent reaction order with respect to water vapor.

The parameter k' was determined to be 0.64 ± 0.02 (normalised units) and represents a dimensionless, device-specific parameter. However, k' is not further discussed here, as no directly comparable data sets are available and the time-dependent reaction dynamics are, as outlined above, strongly device-dependent.

In contrast, the apparent reaction order was determined to be 1.43 ± 0.05, indicating a fractional reaction order with respect to water vapor. Such a non-integer order suggests that the charge-carrier quenching rate increases disproportionately with the trace-humidity concentration ($r \propto [H_2O_{(g)}]^{1.43\pm0.05}$), implying that more than one water molecule is effectively involved in the charge-carrier quenching-relevant process.

Such measurement results are consistent with cooperative adsorption processes and suggest the formation of water-induced clusters, either as MHP–water complexes or as island-like water aggregates on the MHP surface.[82,83] As a result, the pseudo-reaction-rate analysis indicates that charge-carrier quenching under trace humidity conditions is governed by cooperative, water-mediated interactions, rather than by a simple, single-site adsorption process.

To contextualize this kinetic characterization of the humidity-induced quenching process, it is instructive to place the observed photocurrent response into a broader experimental and literature context. Therefore, we would like to briefly highlight a related study by Howard *et al.*, who investigated MHP-based thin films using PL spectroscopy under varying humidity conditions.[84] Their findings revealed a pronounced hysteresis during humidity cycles between >1000 ppm_V and higher levels, leading to irreversible and humidity-induced degradation of the perovskite films.[84]

In contrast, our measurements did not show similar hysteresis or enhanced degradation under trace-humidified conditions. This observation is encouraging, as it suggests that under the low humidity levels investigated in our study, the MHP interacts reversible, enabling a degree of tolerance toward unintended, low-level humidity exposure during device fabrication.

Nonetheless, reversibility observed on our experimental time scales should not be equated with long-term material stability. As discussed above, the pronounced water sensitivity of the MHP, combined with the high mobility of water molecules, implies that even trace amounts of water can repeatedly interact with the material. Over extended operational periods relevant to photovoltaic devices with target lifetimes of approximately 20 years, recurring water-mediated interactions may cumulatively alter intrinsic material properties. Such processes can facilitate corrosion and ultimately compromise device longevity.[52,71–76]

Therefore, while the process appears reversible in the short term, it does not preclude the possibility of cumulative water-induced degradation over long time scales.

Quenching dynamics based on Stern–Volmer model

In the previous sections, the sensitivity and response behaviour of the MHP to trace humidity were discussed in detail. In the following, we focus on the quenching dynamics, which are analysed in terms of charge-carrier populations. For this purpose, first, the classic Stern–Volmer (SV) model[85]

$$\frac{I_0}{I} = 1 + K_{SV} \times [Q] \tag{5}$$

was employed, where I_0 and I denote the emission intensity in the absence and presence of the quencher, respectively, K_{SV} is the Stern–Volmer constant, and [Q] represents the quencher concentration (humidity). In the context of this study, charge-carrier quenching is understood as an effective reduction of the carrier population contributing to (PL-)emission and current density, rather than being restricted to non-radiative recombination alone. While it is not possible to distinguish between carrier losses caused by non-radiative recombination and those arising from transport-related effects, both mechanisms reduce the population of charge carriers contributing to device operation and are therefore treated equivalently within the Stern–Volmer framework. Moreover, under the low current density (low-injection) conditions investigated here, space-charge effects and strong transport nonlinearities are expected to be negligible. Therefore, variations in both the PL intensity and the current density primarily reflect changes in the effective charge-carrier population contributing to radiative emission and charge extraction. Accordingly, PL and current density are used as experimental proxies for the relative carrier population (n),

$$\Delta n \propto \Delta PL \tag{6}$$

and

$$\Delta n \propto \Delta J \tag{7}$$

This approximation provides the physical and methodological basis for applying the Stern–Volmer framework to the current response:

$$\frac{J_0}{J} \propto 1 + K_{SV} \times [Q] \tag{8}$$

In addition to the classical SV model, the two-site SV model was applied, which has already proved to be more effective in characterizing the PL-quenching behaviour of a MHP thin film.[55,86] An equivalent assumption regarding the charge-carrier population was applied here as well:

$$\frac{J_0}{J} \propto \frac{1}{\frac{f_{01}}{1 + K'_{SV1} \times [Q]} + \frac{f_{02}}{1 + K'_{SV2} \times [Q]}} \tag{9}$$

with

$$1 = f_{01} + f_{02} \tag{10}$$

Here, f_{01} and f_{02} are the fractional contributions to the unquenched steady state emission from two components of different accessibility and K'_{SV1} and K'_{SV2} are effective quenching constants.[86]

Fig. 5a presents the J_0/J ratios (see Table S2) in relation to the trace humidity concentrations investigated from Fig. 3. The

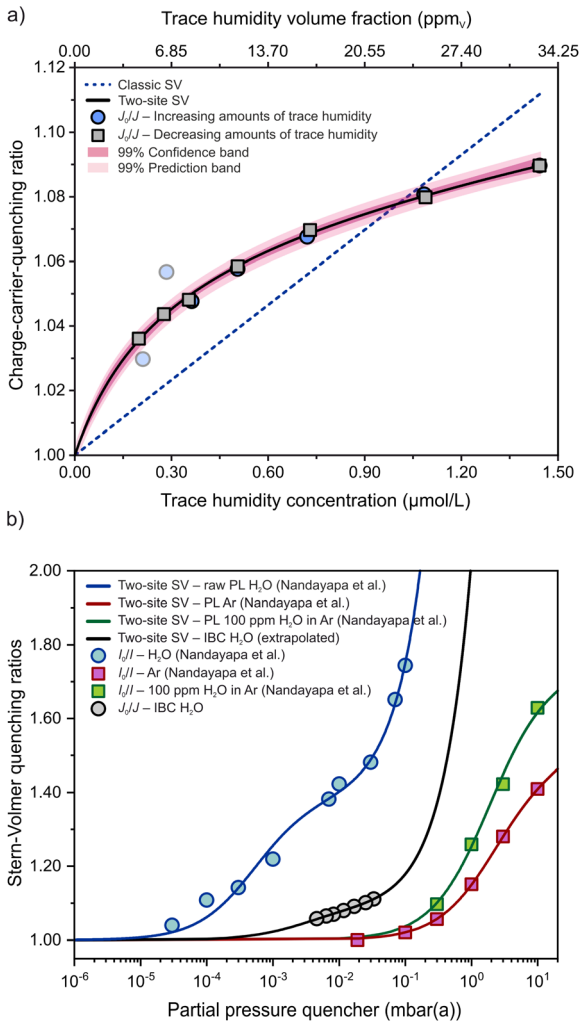

Fig. 5 In (a) are the IBC charge-carrier quenching ratios presented as a function of the investigated trace humidity concentrations (volume fractions), considering both increasing and decreasing amounts of humidity. The charge-carrier quenching ratios obtained for decreasing trace humidity concentrations (high-to-low amounts) were used for the classic SV model fit (dashed blue line). The two-site SV model (black) was applied to all data points expect for the two noisy points shown as more transparent blue dots (low-to-high amounts). Additionally, 99% confidence and prediction bands are shown for the two-site SV fit. (b) Provides a comparative summary of the charge-carrier quenching ratios obtained in this study with our previously reported PL-quenching ratios. For clarity, please note that the x-axis displays only a maximum partial pressure of 15 mbar(a). The PL-quenching ratios acquired under dry argon and trace-humidified argon were used to extract the raw PL response to water vapor. This response is directly compared to the IBC charge-carrier quenching ratios, facilitating a deeper understanding of the quenching behaviour across different measurement techniques.

ratios for both increasing and decreasing trace humidity concentrations show excellent agreement, further confirming that the charge-carrier quenching is fully reversible within the explored timescale and conditions, despite degradation behaviour. Due to the noise observed in the first two phases from low-to-high trace-humidity volume fractions, the readings from high-to-low trace-humidity volume fractions were analysed using the classic SV analysis. For the two-site SV analysis, all data points from both trace-humidity measurement directions were included, except for the two noisy points from the low-to-high trace-humidity series (shown as more transparent blue dots). Consequently, a total of 11 data points were used for the two-site SV analysis. The classic SV plot is shown in blue (dashed line) and the two-site SV plot in black, with the corresponding 99% confidence and prediction bands (displayed in red). The two-site model provides a significantly better fit to the experimental data.

Generally, the classical SV model assumes homogeneous quenching with a single quenching constant, implying a constant quenching efficiency per quencher molecule over the entire concentration range. However, the measured current density ratios exhibit a pronounced non-linear dependence, characterized by an enhanced quenching response at low humidity levels followed by a gradual increase at higher concentrations. This behaviour cannot be captured by a linear SV description and indicates the presence of at least two kinetically distinct quenching pathways with different accessibility to water.

In contrast, the non-linear two-site SV model accounts for heterogeneous quenching by covering two contributions with different quenching accessibilities. The relatively narrow 99% confidence and prediction bands indicate that the two-site SV model provides an excellent description of the experimental data over the investigated volume fraction range. Moreover, the use of data obtained from both measurement directions suggests that the parameter estimation is reasonably robust. Including the two noisy data points would primarily increase the uncertainty of the estimated model parameters, without affecting the conclusions derived from these parameters (discussed in the following). In addition, the confidence and prediction bands obtained from the fit based on 11 data points indicate their treatment as outliers. Therefore, the excellent agreement obtained using this model suggests that the charge-carrier quenching in MHP-based IBC solar cells is characterized by heterogeneous and site-dependent interactions with trace humidity, analogous to the non-linear PL-quenching behaviour previously reported for MHP thin films.[55]

Fig. 5b presents a direct, comparative analysis of SV quenching ratios derived from two distinct but complementary data sets. The charge-carrier quenching ratios observed in this study are shown alongside previously reported PL quenching ratios (ref. 55), which were obtained by setting static partial pressures starting from high vacuum. Please note that the *x*-axis (quencher partial pressure) is shown on a logarithmic scale and restricted to the relevant range. Further, all data points were evaluated using only the two-site SV model.

The grey data points represent the charge-carrier quenching ratios obtained in this study, including an extrapolation to higher water vapor partial pressures. The remaining data sets, shown in blue, green, and red, correspond to our previously reported PL quenching measurements.[55] Specifically, the red data set shows PL-quenching ratios measured in dry argon (quencher = Ar), while the green data set represents PL-quenching ratios obtained in an argon gas mixture containing 100 ppm trace humidity (quencher = Ar + H_2O).

The blue data set represents the PL-quenching contribution attributed only to water vapor. These values were obtained by comparing PL-quenching ratios measured in dry argon and humidified argon, with the resulting differences plotted on the *y*-axis. The corresponding water vapor partial pressures were calculated from the partial pressures of the humid argon gas standard by applying Dalton's law, yielding the partial pressure of water vapor alone (*i.e.*, excluding the argon contribution).

In contrast, for the IBC measurements, the water vapor partial pressure was directly derived from the measured frost point temperatures, providing a highly precise and traceable thermodynamic determination.[65] Additionally, it is important to note that the IBC measurements were conducted under a continuous gas flow of clean and dry nitrogen, with trace humidity phases. As a result, the obtained charge-carrier quenching ratios are entirely independent of the surrounding nitrogen gas matrix. This independence arises because nitrogen consistently induces a background charge-carrier quenching effect on the MHP, ensuring that any additional quenching is solely attributed to the introduced quencher – water.

Table 1 summarizes the two-site SV parameters obtained for the IBC solar cell, including the uncertainties of the fit parameters and the coefficient of determination (R^2), and compares them with our previously reported PL results (ref. 55). A direct comparison between row 1 (IBC charge-carrier quenching ratios from Fig. 5a) and row 2 (PL-quenching ratios of humidity in argon; ref. 55) reveals pronounced differences in the relative contributions of the two quenching sites.

In the IBC solar cell, the fraction of so-called "easy-to-quench sites" (f_{01}), which within this model are typically associated with surface-related quenching processes, account to only 7%. In contrast, PL measurements exhibit a substantially larger contribution of these sites, with f_{01} = 44%. At this point, we would like to emphasize that these interpretations are model-based and do not represent direct structural identification.

Nevertheless, this discrepancy can be attributed primarily to the different gas environments used in the two experiments. In the PL measurements, argon—with a molar fraction of 99.99 cmol mol^{-1}—acts as a dominant background quencher, despite water being intrinsically the stronger quencher.[55] Consequently, surface-related quenching is more prominently reflected in the PL response (argon-like quenching behaviour).

By contrast, charge-carrier quenching in the IBC solar cell is dominated by "hard-to-quench sites" (f_{02} = 92%), whose physical interpretation within the two-site SV model is discussed in more detail below. As a result, we conclude that the quenching constants between these two measurements are not directly comparable.

Table 1 An overview of the two-site SV parameters from Fig. 5. Uncertainties are reported at a 95% confidence interval

		f_{01}	K'_{SV1} (L mol^{-1})	f_{02}	K'_{SV2} (L mol^{-1})	R^2
1	IBC (Fig. 5a)	0.078 ± 0.006	3 240 070.8 ± 383 727.2	0.922 ± 0.006	13 789.4 ± 2867.5	0.9982
2	PL – ref. 55 (H_2O in Ar)	0.44	17 303.2	0.56	6.5	—
		f_{01}	K'_{SV1} (mbar(a)$^{-1}$)	f_{02}	K'_{SV2} (mbar(a)$^{-1}$)	R^2
3	Raw PL of H_2O	0.278 ± 0.011	2645.1 ± 596.4	0.722 ± 0.011	2.67 ± 0.28	0.9925
4	IBC H_2O	0.080 ± 0.005	356.1 ± 56.0	0.920 ± 0.005	0.87 ± 0.13	0.9977

To overcome this comparability limitation, the PL data were reprocessed as discussed above (row 3 of Table 1) to ensure that water vapor is treated as the only effective quencher in the PL analysis. Also, as discussed above, charge-carrier quenching in the IBC measurements is solely attributed to water vapor (row 4 of Table 1).

This harmonized treatment enables a direct comparison of the two SV analyses, despite the measurements being performed at different timelines, by different operators, and using two fundamentally different methods – both in terms of quenching dynamics (PL-quenching *vs.* charge-carrier quenching) and experimental setup (static partial pressures *vs.* continuous dynamic dilution).

A comparison of the quenching site distributions reveals that "hard-to-quench sites" dominate in both measurement approaches, accounting for 92% for the IBC charge-carrier quenching and 72% for PL-quenching. The larger contribution of "hard-to-quench sites" observed in the IBC measurements is attributed to the fundamentally different probing depths of the two analytical techniques.

PL spectroscopy can be regarded as a predominantly two-dimensional (2D) probe, as it is primarily sensitive to the surface and near-surface regions of the perovskite layer and thus mainly provide information about the recombination mechanisms of charge carriers and defect states.[87,88] In contrast, current density measurements describe the extraction of charge carriers at the electrodes, representing not only the perovskite surface but also the bulk and interface-near regions. As a result, IBC charge-carrier quenching provides a more comprehensive, three-dimensional (3D) perspective on quenching processes within the device. This difference in measurement dimensionality explains why surface-related quenching contributes 28% to the PL response, whereas it accounts for only 8% in the IBC measurements.

Based on these results, the model-based definition of the "hard-to-quench" sites requires further contextualization. In our previous PL-based publication, these sites were primarily associated with grain boundaries.[55] In the present case, however, such a direct assignment is less appropriate for the charge-carrier quenching response measured at the device level, since the current–density response represents an integrated signal comprising charge transport, recombination, and extraction across the entire device. Accordingly, the measured response may be influenced not only by grain boundaries, but also by bulk traps, buried interfaces, transport barriers, and contact-limited extraction processes. Within the framework of the two-site SV model, the f_{02} parameter describes the fractional contribution of sites with lower accessibility in the unquenched steady-state response. Thus, in the context of the current density measurements, f_{02} is more appropriately interpreted as representing less directly accessible quenching sites within the device, reflecting the distinct transport and extraction pathways probed by *J–V* measurements.

Beyond the qualitative interpretation of f_{02}, comparing the ratios of K'_{SV1} to K'_{SV2} provides an additional quantitative perspective and reveals that surface crystallites exhibit 2.4-times higher quenching sensitivity in PL measurements than in *J–V* measurements. This discrepancy is most likely attributed to the above-discussed differences in analytical measurement techniques, as well as variations in MHP surface properties (see SI for IBC surface topography).

Further support for these interpretations is provided by our water outgassing results, which demonstrate that water is highly mobile within the perovskite layer. In this context, however, the perovskite behaves like a sponge, accommodating water not only at the surface but also in the near-surface region and other less directly accessible regions of the MHP, thereby enhancing quenching contributions from "hard-to-quench sites" in device-level measurements. Notably, the interpretation of the experimental observations based on the corresponding two-site SV analyses are in close agreement with theoretical predictions reported in the literature,[89] further supporting both the conclusions drawn in this study and our previously reported findings.

These insights highlight the quality of grain-boundary junctions and device interfaces as a critical factor for device stability and the preservation of intrinsic material properties. Consequently, targeted passivation strategies aimed at stabilizing grain boundaries and buried interfaces represent a promising route to enhance long-term operational stability.[90–95] In particular, embedding passivation materials within the MHP that are capable of adsorbing and temporarily storing water, or facilitating material recovery upon water outgassing, can mitigate humidity-induced degradation. Such

approaches include, for example, polymeric epoxy curing reactions[96] or the incorporation of hindered urea-based Lewis acid materials[97] to protect grain-boundary junctions against extrinsic stressors.

Trace humidity guideline value determination

A trace-humidity guideline value derived from our study must be interpreted as a material-intrinsic sensitivity limit, rather than a device-performance metric. The investigated IBC solar cells exhibit low charge extraction and are fully unencapsulated. This configuration minimizes secondary effects such as interface corrosion, and water accumulation, thereby isolating the direct interaction between water vapor and the MHP under low-injection conditions. Moreover, the open IBC architecture was deliberately chosen to permit unobstructed water migration and to use the photocurrent primarily as a sensitive probe of humidity-induced charge-carrier quenching rather than as a representative photovoltaic performance metric.

The two-site SV analysis was applied as a model system and demonstrates that cooperative, water-mediated charge-carrier quenching already occurs at trace humidity levels well below 10 ppm_V and is dominated by interactions at less directly accessible quenching sites within the device. These quenching sites are intrinsic to polycrystalline MHP and are therefore expected to be present in all device architectures.

In contrast to the open IBC configuration, conventional sandwich-type perovskite solar cells feature embedded architectures with multiple water-sensitive interfaces and significantly higher internal electric fields. Under such conditions, incorporated water may interact more persistently with the MHP and its interfaces, potentially amplifying both quenching and cumulative degradation processes. Accordingly, the present IBC devices should be regarded as a simplified model system for identifying an intrinsic lower-bound indicator of water–perovskite interactions, rather than a universally transferable processing criterion for all solar cell architectures.

At the same time, however, the pronounced sensitivity of MHPs to trace humidity implies that even low water vapor volume fractions can lead to measurable uptake of water by the material. Under realistic fabrication conditions, the perovskite layer is expected to establish a dynamic equilibrium between water associated with the perovskite and water molecules in the surrounding gas atmosphere. Consequently, even when devices are fabricated in environments with low humidity levels, a finite amount of water can become incorporated within the perovskite layer. Once incorporated, these water molecules may repeatedly interact with the perovskite lattice and its interfaces, potentially leading to cumulative effects over extended operational times.

The experimentally observed quenching response at trace humidity levels therefore highlights that even very low water vapor volume fractions in the fabrication atmosphere and during encapsulation can already lead to water incorporation and subsequent interactions within the device. Based on this consideration, trace humidity levels of ≤ 5 ppm_V substantially reduce, but do not fully suppress, water-induced interactions, while a further reduction to sub-ppm levels leads to a significant weakening of cooperative water interactions. According to the two-site SV analysis, humidity levels around (0.96 ± 0.12) ppm_V (expanded measurement uncertainty at 95%) correspond to a charge-carrier quenching of 1%. This level is not interpreted as a strict physical threshold, but rather as a practically meaningful lower-bound guideline associated with only a minor residual interaction, acknowledging that completely water-free processing conditions are neither experimentally nor technologically achievable due to the omnipresence of water in gases, materials, and processing environments. A residual interaction on the order of $\leq$1% therefore represents a realistic lower limit and is reliably met by nitrogen of quality grade 6.0, which is technically well established and readily implementable in both laboratory and industrial fabrication environments. Furthermore, based on our experience of routinely quantifying trace humidity volume fractions of approximately 0.3 ppm_V in nitrogen 6.0, the use of this purity grade can be assumed to provide a practical buffer to our specified intrinsic limit. Furthermore, commercially available and well-established gas purification systems enable the reduction of trace humidity in nitrogen from grade 5.0 or lower to the identified guideline level and under controlled conditions, to even substantially lower trace-humidity levels ($\leq$0.3 ppm_V).

Therefore, a humidity level of approximately (0.96 ± 0.12) ppm_V should be regarded as a physically justified and technologically meaningful model-based lower-bound guideline value for minimizing water uptake during fabrication and encapsulation and, consequently, for reducing cumulative water-induced degradation processes within the device under realistic operation.

Conclusions

In this study, we investigated the impact of trace humidity on unencapsulated, fully unembedded MHP-based IBC solar cells during operation. We probed trace humidity volume fractions ranging from approximately 5 ppm_V to 34 ppm_V, whereby the trace humidity quantification was traced back to national standards using a transfer standard dew point hygrometer. Our observation of water outgassing from the perovskite layer indicates a significant Joule heating process during operation. A notable charge-carrier quenching was observed, even at a low trace humidity volume fraction of about 5 ppm_V. Moreover, we observed that 92% of the charge-carrier quenching occurs at less directly accessible quenching sites within the device and that the photocurrent recovers in trace-humidified condition. Although the quenching and response behaviour of the perovskite is determined to be reversible within the explored timescale, the material exhibited a very high sensitivity to humidity changes. Despite the reversible nature of these effects in the short term, we discussed intrinsic changes in the material properties. In addition, water migration through the MHP layer was identified, which may lead to corrosion processes at the metal electrode interfaces in traditional embedded device architectures and/or to decreasing MHP phase stability.

Moreover, the two-site Stern–Volmer model was applied to describe how strongly trace humidity influences the charge

carrier population. Based on this model-based interpretation we were able to quantify an intrinsic lower-bound guideline value of water–perovskite interactions relevant to the fabrication and encapsulation of perovskite solar cells. Our results suggest that maintaining trace-humidity volume fractions at around (0.96 ± 0.12) ppm_V during fabrication and encapsulation is required for preserving the intrinsic properties of the MHP. This clearly demonstrates the sensitivity of MHP to trace humidity and underlines the necessity of controlling and minimizing trace humidity volume fractions in the gas atmosphere during the fabrication and encapsulation process of perovskite solar cells.

Author contributions

Mehmet E. Bayat data curation, formal analysis, investigation, methodology, visualization, writing – original draft; Edgar R. Nandayapa software, formal analysis, writing – review & editing; Carlo Tiebe methodology, validation, resources, supervision, writing – review & editing; Eva L. Unger conceptualization, methodology, writing – review & editing; Emil J. W. List-Kratochvil conceptualization, methodology, project administration, resources, supervision, funding acquisition, writing – review & editing.

Conflicts of interest

There are no conflicts to declare.

Data availability

All data are available within the article, and at https://doi.org/10.5281/zenodo.18600852.

Supplementary information (SI): device preparation; experimental setup; layer characterization; device topography; IBC solar cell characterization; water outgassing; deposited MHP mass calculation on the active area; sample gases; baseline correction methodology; and quenching ratios. See DOI: https://doi.org/10.1039/d6ta01295g.

Acknowledgements

The authors acknowledge the funding by the Helmholtz Energy Materials Foundry. We thank Harald Kohlhoff and Jessica Erdmann for the fabrication of the IBC sample holder. We thank Dr Vincent Schröder and Dr Felix Hermerschmidt for constructive discussions. This work was carried out in the framework of the joint lab for generative manufacturing processes for hybrid components (GenFab).

References

1 L. Schmidt-Mende, V. Dyakonov, S. Olthof, F. Ünlü, K. M. T. Lê, S. Mathur, A. D. Karabanov, D. C. Lupascu, L. M. Herz, A. Hinderhofer, F. Schreiber, A. Chernikov, D. A. Egger, O. Shargaieva, C. Cocchi, E. Unger, M. Saliba, M. M. Byranvand, M. Kroll, F. Nehm, K. Leo, A. Redinger, J. Höcker, T. Kirchartz, J. Warby, E. Gutierrez-Partida, D. Neher, M. Stolterfoht, U. Würfel, M. Unmüssig, J. Herterich, C. Baretzky, J. Mohanraj, M. Thelakkat, C. Maheu, W. Jaegermann, T. Mayer, J. Rieger, T. Fauster, D. Niesner, F. Yang, S. Albrecht, T. Riedl, A. Fakharuddin, M. Vasilopoulou, Y. Vaynzof, D. Moia, J. Maier, M. Franckevičius, V. Gulbinas, R. A. Kerner, L. Zhao, B. P. Rand, N. Glück, T. Bein, F. Matteocci, L. A. Castriotta, A. Di Carlo, M. Scheffler and C. Draxl, *APL Mater.*, 2021, **9**, 109202.

2 M. Saliba, J.-P. Correa-Baena, C. M. Wolff, M. Stolterfoht, N. Phung, S. Albrecht, D. Neher and A. Abate, *Chem. Mater.*, 2018, **30**, 4193–4201.

3 E. Unger and J. T. Jacobsson, *ACS Energy Lett.*, 2022, **7**, 1240–1245.

4 J. Li, J. Dagar, O. Shargaieva, O. Maus, M. Remec, Q. Emery, M. Khenkin, C. Ulbrich, F. Akhundova, J. A. Márquez, T. Unold, M. Fenske, C. Schultz, B. Stegemann, A. Al-Ashouri, S. Albrecht, A. T. Esteves, L. Korte, H. Köbler, A. Abate, D. M. Többens, I. Zizak, E. J. W. List-Kratochvil, R. Schlatmann and E. Unger, *Adv. Energy Mater.*, 2023, **13**, 2203898.

5 A. Tara, V. Schröder, A. Paul, N. Maticiuc, M. F. Vasquez-Montoya, J. Dagar, S. Sharma, R. Gupta, E. J. W. List-Kratochvil, E. L. Unger and F. Mathies, *ACS Appl. Mater. Interfaces*, 2024, **16**, 63520–63527.

6 E. L. Unger, A. R. Bowring, C. J. Tassone, V. L. Pool, A. Gold-Parker, R. Cheacharoen, K. H. Stone, E. T. Hoke, M. F. Toney and M. D. McGehee, *Chem. Mater.*, 2014, **26**, 7158–7165.

7 V. R. F. Schröder, N. Fratzscher, N. Zorn Morales, D. S. Rühl, F. Hermerschmidt, E. L. Unger and E. J. W. List-Kratochvil, *Mater. Horiz.*, 2024, **11**, 1989–1996.

8 X.-K. Liu, W. Xu, S. Bai, Y. Jin, J. Wang, R. H. Friend and F. Gao, *Nat. Mater.*, 2021, **20**, 10–21.

9 F. Hermerschmidt, F. Mathies, V. R. F. Schröder, C. Rehermann, N. Z. Morales, E. L. Unger and E. J. W. List-Kratochvil, *Mater. Horiz.*, 2020, **7**, 1773–1781.

10 K. Lê, F. von Toperczer, F. Ünlü, G. Paramasivam, F. Mathies, E. Nandayapa, E. J. W. List-Kratochvil, T. Fischer, K. Lindfors and S. Mathur, *Adv. Eng. Mater.*, 2023, **25**, 2201651.

11 V. R. F. Schröder, N. Fratzscher, F. Mathies, E. R. Nandayapa, F. Hermerschmidt, E. L. Unger and E. J. W. List-Kratochvil, *Nanoscale*, 2023, **15**, 5649–5654.

12 X. Zhang, C. Ji, X. Liu, S. Wang, L. Li, Y. Peng, Y. Yao, M. Hong and J. Luo, *Adv. Opt. Mater.*, 2020, **8**, 2000311.

13 H.-P. Wang, S. Li, X. Liu, Z. Shi, X. Fang and J.-H. He, *Adv. Mater.*, 2021, **33**, 2003309.

14 R. Ollearo, J. Wang, M. J. Dyson, C. H. L. Weijtens, M. Fattori, B. T. van Gorkom, A. J. J. M. van Breemen, S. C. J. Meskers, R. A. J. Janssen and G. H. Gelinck, *Nat. Commun.*, 2021, **12**, 7277.

15 M. Zhang, F. Zhang, Y. Wang, L. Zhu, Y. Hu, Z. Lou, Y. Hou and F. Teng, *Sci. Rep.*, 2018, **8**, 11157.

16 F. Bella, G. Griffini, J.-P. Correa-Baena, G. Saracco, M. Grätzel, A. Hagfeldt, S. Turri and C. Gerbaldi, *Science*, 2016, **354**, 203–206.

17 Q. Emery, M. Remec, G. Paramasivam, S. Janke, J. Dagar, C. Ulbrich, R. Schlatmann, B. Stannowski, E. Unger and M. Khenkin, *ACS Appl. Mater. Interfaces*, 2022, **14**, 5159–5167.
18 M. Khenkin, H. Köbler, M. Remec, R. Roy, U. Erdil, J. Li, N. Phung, G. Adwan, G. Paramasivam, Q. Emery, E. Unger, R. Schlatmann, C. Ulbrich and A. Abate, *Energy Environ. Sci.*, 2024, **17**, 602–610.
19 M. V. Khenkin, E. A. Katz, A. Abate, G. Bardizza, J. J. Berry, C. Brabec, F. Brunetti, V. Bulović, Q. Burlingame, A. Di Carlo, R. Cheacharoen, Y.-B. Cheng, A. Colsmann, S. Cros, K. Domanski, M. Dusza, C. J. Fell, S. R. Forrest, Y. Galagan, D. Di Girolamo, M. Grätzel, A. Hagfeldt, E. von Hauff, H. Hoppe, J. Kettle, H. Köbler, M. S. Leite, S. Liu, Y.-L. Loo, J. M. Luther, C.-Q. Ma, M. Madsen, M. Manceau, M. Matheron, M. McGehee, R. Meitzner, M. K. Nazeeruddin, A. F. Nogueira, Ç. Odabaşı, A. Osherov, N.-G. Park, M. O. Reese, F. De Rossi, M. Saliba, U. S. Schubert, H. J. Snaith, S. D. Stranks, W. Tress, P. A. Troshin, V. Turkovic, S. Veenstra, I. Visoly-Fisher, A. Walsh, T. Watson, H. Xie, R. Yıldırım, S. M. Zakeeruddin, K. Zhu and M. Lira-Cantu, *Nat. Energy*, 2020, **5**, 35–49.
20 M. Saliba, T. Matsui, J.-Y. Seo, K. Domanski, J.-P. Correa-Baena, M. K. Nazeeruddin, S. M. Zakeeruddin, W. Tress, A. Abate, A. Hagfeldt and M. Grätzel, *Energy Environ. Sci.*, 2016, **9**, 1989–1997.
21 J. J. Yoo, G. Seo, M. R. Chua, T. G. Park, Y. Lu, F. Rotermund, Y.-K. Kim, C. S. Moon, N. J. Jeon, J.-P. Correa-Baena, V. Bulović, S. S. Shin, M. G. Bawendi and J. Seo, *Nature*, 2021, **590**, 587–593.
22 M. M. Tavakoli, P. Yadav, D. Prochowicz, M. Sponseller, A. Osherov, V. Bulović and J. Kong, *Adv. Energy Mater.*, 2019, **9**, 1803587.
23 S. F. Solari, L.-N. Poon, M. Wörle, F. Krumeich, Y.-T. Li, Y.-C. Chiu and C.-J. Shih, *J. Am. Chem. Soc.*, 2022, **144**, 5864–5870.
24 C. Otero-Martínez, N. Fiuza-Maneiro and L. Polavarapu, *ACS Appl. Mater. Interfaces*, 2022, **14**, 34291–34302.
25 T. Bu, L. Wu, X. Liu, X. Yang, P. Zhou, X. Yu, T. Qin, J. Shi, S. Wang, S. Li, Z. Ku, Y. Peng, F. Huang, Q. Meng, Y.-B. Cheng and J. Zhong, *Adv. Energy Mater.*, 2017, **7**, 1700576.
26 D. Yang, X. Zhou, R. Yang, Z. Yang, W. Yu, X. Wang, C. Li, S. Liu and R. P. H. Chang, *Energy Environ. Sci.*, 2016, **9**, 3071–3078.
27 S. Wang, H. Chen, J. Zhang, G. Xu, W. Chen, R. Xue, M. Zhang, Y. Li and Y. Li, *Adv. Mater.*, 2019, **31**, 1903691.
28 Y.-D. Wang, Y. Wang, J.-Y. Shao, Y. Lan, Z.-R. Lan, Y.-W. Zhong and Y. Song, *ACS Energy Lett.*, 2021, **6**, 2030–2037.
29 L. Qiu, L. K. Ono, Y. Jiang, M. R. Leyden, S. R. Raga, S. Wang and Y. Qi, *J. Phys. Chem. B*, 2018, **122**, 511–520.
30 Q. Dong, C. Zhu, M. Chen, C. Jiang, J. Guo, Y. Feng, Z. Dai, S. K. Yadavalli, M. Hu, X. Cao, Y. Li, Y. Huang, Z. Liu, Y. Shi, L. Wang, N. P. Padture and Y. Zhou, *Nat. Commun.*, 2021, **12**, 973.
31 X. Wang, W. Wang, J. Liu, J. Qi, Y. He, Y. Wang, W. Hu, Y. Cheng, K. Chen, Y. Hu, A. Mei and H. Han, *Adv. Funct. Mater.*, 2022, **32**, 2203872.
32 Y. Zhang, Z. Yang, T. Ma, Z. Ai, Y. Bao, L. Shi, L. Qin, G. Cao, C. Wang and X. Li, *Small Sci.*, 2024, **4**, 2300188.
33 A. Ali, M. J. Cha, J. H. Kang, Y. J. Park, J. H. Seo and B. Walker, *Adv. Eng. Mater.*, 2020, **22**, 2000185.
34 C. Momblona, L. Gil-Escrig, E. Bandiello, E. M. Hutter, M. Sessolo, K. Lederer, J. Blochwitz-Nimoth and H. J. Bolink, *Energy Environ. Sci.*, 2016, **9**, 3456–3463.
35 M. Casareto and N. Rolston, *Commun. Mater.*, 2024, **5**, 74.
36 H. Li, Y. Peng, W. Zhou, J. Guo, C. Gao, Y. He, M. Pan, C. Yang and H. Huang, *ACS Appl. Mater. Interfaces*, 2024, **16**, 36471–36478.
37 S. Liu, V. P. Biju, Y. Qi, W. Chen and Z. Liu, *NPG Asia Mater.*, 2023, **15**, 27.
38 Y. Qian, J. Li, H. Cao, Z. Ren, X. Dai, T. Huang, S. Zhang, Y. Qiu, L. Yang and S. Yin, *Adv. Funct. Mater.*, 2023, **33**, 2214731.
39 S. Zhang and G. Han, *Prog. Energy*, 2020, **2**, 022002.
40 M. Ralaiarisoa, I. Salzmann, F.-S. Zu and N. Koch, *Adv. Electron. Mater.*, 2018, **4**, 1800307.
41 J. Hidalgo, W. Kaiser, Y. An, R. Li, Z. Oh, A.-F. Castro-Méndez, D. K. LaFollette, S. Kim, B. Lai, J. Breternitz, S. Schorr, C. A. R. Perini, E. Mosconi, F. De Angelis and J.-P. Correa-Baena, *J. Am. Chem. Soc.*, 2023, **145**, 24549–24557.
42 N. Ahn, K. Kwak, M. S. Jang, H. Yoon, B. Y. Lee, J.-K. Lee, P. V. Pikhitsa, J. Byun and M. Choi, *Nat. Commun.*, 2016, **7**, 13422.
43 N. Aristidou, I. Sanchez-Molina, T. Chotchuangchutchaval, M. Brown, L. Martinez, T. Rath and S. A. Haque, *Angew. Chem., Int. Ed.*, 2015, **54**, 8208–8212.
44 N. Aristidou, C. Eames, I. Sanchez-Molina, X. Bu, J. Kosco, M. S. Islam and S. A. Haque, *Nat. Commun.*, 2017, **8**, 15218.
45 X. Gong, M. Li, X.-B. Shi, H. Ma, Z.-K. Wang and L.-S. Liao, *Adv. Funct. Mater.*, 2015, **25**, 6671–6678.
46 S. Xiao, K. Zhang, S. Zheng and S. Yang, *Nanoscale Horiz.*, 2020, **5**, 1147–1154.
47 N. Adhikari, A. Dubey, E. A. Gaml, B. Vaagensmith, K. M. Reza, S. A. A. Mabrouk, S. Gu, J. Zai, X. Qian and Q. Qiao, *Nanoscale*, 2016, **8**, 2693–2703.
48 K. Liu, Y. Luo, Y. Jin, T. Liu, Y. Liang, L. Yang, P. Song, Z. Liu, C. Tian, L. Xie and Z. Wei, *Nat. Commun.*, 2022, **13**, 4891.
49 K. Sun, R. Guo, Y. Liang, J. E. Heger, S. Liu, S. Yin, M. A. Reus, L. V. Spanier, F. Deschler, S. Bernstorff and P. Müller-Buschbaum, *ACS Appl. Mater. Interfaces*, 2023, **15**, 30342–30349.
50 J. S. Yun, J. Kim, T. Young, R. J. Patterson, D. Kim, J. Seidel, S. Lim, M. A. Green, S. Huang and A. Ho-Baillie, *Adv. Funct. Mater.*, 2018, **28**, 1705363.
51 W.-C. Lin, H.-Y. Chang, K. Abbasi, J.-J. Shyue and C. Burda, *Adv. Mater. Interfaces*, 2017, **4**, 1600673.
52 Y. Han, S. Meyer, Y. Dkhissi, K. Weber, J. M. Pringle, U. Bach, L. Spiccia and Y.-B. Cheng, *J. Mater. Chem. A*, 2015, **3**, 8139–8147.

53 D. R. Ceratti, A. Zohar, R. Kozlov, H. Dong, G. Uraltsev, O. Girshevitz, I. Pinkas, L. Avram, G. Hodes and D. Cahen, *Adv. Mater.*, 2020, **32**, 2002467.
54 W. H. Schön, in *Handbuch der Reinsten Gase*, Springer Berlin Heidelberg, Berlin, Heidelberg, 2005, pp. 1–9, DOI: 10.1007/3-540-27654-8_1.
55 E. R. Nandayapa, K. Hirselandt, C. Boeffel, E. L. Unger and E. J. W. List-Kratochvil, *Adv. Opt. Mater.*, 2021, **9**, 2001317.
56 T. Ma, Q. Song, D. Tadaki, M. Niwano and A. Hirano-Iwata, *ACS Appl. Energy Mater.*, 2018, **1**, 970–975.
57 M. Alsari, O. Bikondoa, J. Bishop, M. Abdi-Jalebi, L. Y. Ozer, M. Hampton, P. Thompson, M. T. Hörantner, S. Mahesh, C. Greenland, J. E. Macdonald, G. Palmisano, H. J. Snaith, D. G. Lidzey, S. D. Stranks, R. H. Friend and S. Lilliu, *Energy Environ. Sci.*, 2018, **11**, 383–393.
58 L. M. Pazos-Outón, M. Szumilo, R. Lamboll, J. M. Richter, M. Crespo-Quesada, M. Abdi-Jalebi, H. J. Beeson, M. Vrućinić, M. Alsari, H. J. Snaith, B. Ehrler, R. H. Friend and F. Deschler, *Science*, 2016, **351**, 1430–1433.
59 X. Lin, A. S. R. Chesman, S. R. Raga, A. D. Scully, L. Jiang, B. Tan, J. Lu, Y.-B. Cheng and U. Bach, *Adv. Funct. Mater.*, 2018, **28**, 1805098.
60 X. Lin, A. N. Jumabekov, N. N. Lal, A. R. Pascoe, D. E. Gómez, N. W. Duffy, A. S. R. Chesman, K. Sears, M. Fournier, Y. Zhang, Q. Bao, Y.-B. Cheng, L. Spiccia and U. Bach, *Nat. Commun.*, 2017, **8**, 613.
61 G. DeLuca, A. N. Jumabekov, Y. Hu, A. N. Simonov, J. Lu, B. Tan, G. W. P. Adhyaksa, E. C. Garnett, E. Reichmanis, A. S. R. Chesman and U. Bach, *ACS Appl. Energy Mater.*, 2018, **1**, 4473–4478.
62 X. Lin, S. R. Raga, A. S. R. Chesman, Q. Ou, L. Jiang, Q. Bao, J. Lu, Y.-B. Cheng and U. Bach, *Nano Energy*, 2020, **67**, 104223.
63 S. Deng, B. Tan, A. S. R. Chesman, J. Lu, D. P. McMeekin, Q. Ou, A. D. Scully, S. R. Raga, K. J. Rietwyk, A. Weissbach, B. Zhao, N. H. Voelcker, Y.-B. Cheng, X. Lin and U. Bach, *Nano Energy*, 2022, **102**, 107695.
64 A. N. Jumabekov, J. A. Lloyd, D. M. Bacal, U. Bach and A. S. R. Chesman, *ACS Appl. Energy Mater.*, 2018, **1**, 1077–1082.
65 D. Sonntag, *Z. Meteorol.*, 1990, **70**, 340–344.
66 ISO 14912:2025, Gas analysis – Conversion of gas mixture composition data, International Organization for Standardization, Geneva, 2025, https://www.iso.org/standard/85580.html.
67 W. Wagner and A. Pruß, *J. Phys. Chem. Ref. Data*, 2002, **31**, 387–535.
68 J. Pichlmaier, *Tech. Mess.*, 1991, **58**, 471–477.
69 M. E. Bayat, H. Kipphardt, C. Tiebe, D. Tuma and C. Engelhard, *ACS Meas. Sci. Au*, 2025, **5**, 897–911.
70 N. H. Nickel, F. Lang, V. V. Brus, O. Shargaieva and J. Rappich, *Adv. Electron. Mater.*, 2017, **3**, 1700158.
71 L. Li, Z. Guo, R. Fan and H. Zhou, *Nanoscale*, 2023, **15**, 8473–8490.
72 S. Guo, X. Sun, C. Ding, R. Huang, M. Tan, L. Zhang, Q. Luo, F. Li, J. Jin and C.-Q. Ma, *Energy Technol.*, 2020, **8**, 2000250.
73 Y. Kato, L. K. Ono, M. V. Lee, S. Wang, S. R. Raga and Y. Qi, *Adv. Mater. Interfaces*, 2015, **2**, 1500195.
74 U.-G. Jong, C.-J. Yu, G.-C. Ri, A. P. McMahon, N. M. Harrison, P. R. F. Barnes and A. Walsh, *J. Mater. Chem. A*, 2018, **6**, 1067–1074.
75 J. Di, H. Li, J. Su, H. Yuan, Z. Lin, K. Zhao, J. Chang and Y. Hao, *Advanced Science*, 2022, **9**, 2103482.
76 S. Wu, Z. Li, M.-Q. Li, Y. Diao, F. Lin, T. Liu, J. Zhang, P. Tieu, W. Gao, F. Qi, X. Pan, Z. Xu, Z. Zhu and A. K. Y. Jen, *Nat. Nanotechnol.*, 2020, **15**, 934–940.
77 S. Ruan, M.-A. Surmiak, Y. Ruan, D. P. McMeekin, H. Ebendorff-Heidepriem, Y.-B. Cheng, J. Lu and C. R. McNeill, *J. Mater. Chem. C*, 2019, **7**, 9326–9334.
78 B. Conings, J. Drijkoningen, N. Gauquelin, A. Babayigit, J. D'Haen, L. D'Olieslaeger, A. Ethirajan, J. Verbeeck, J. Manca, E. Mosconi, F. D. Angelis and H.-G. Boyen, *Adv. Energy Mater.*, 2015, **5**, 1500477.
79 G. Divitini, S. Cacovich, F. Matteocci, L. Cinà, A. Di Carlo and C. Ducati, *Nat. Energy*, 2016, **1**, 15012.
80 A. Dualeh, N. Tétreault, T. Moehl, P. Gao, M. K. Nazeeruddin and M. Grätzel, *Adv. Funct. Mater.*, 2014, **24**, 3250–3258.
81 Q.-M. Hong, R.-P. Xu, T.-Y. Jin, J.-X. Tang and Y.-Q. Li, *Org. Electron.*, 2019, **67**, 19–25.
82 A. Hodgson and S. Haq, *Surf. Sci. Rep.*, 2009, **64**, 381–451.
83 S. Cheng and H. Zhong, *J. Phys. Chem. Lett.*, 2022, **13**, 2281–2290.
84 J. M. Howard, E. M. Tennyson, S. Barik, R. Szostak, E. Waks, M. F. Toney, A. F. Nogueira, B. R. A. Neves and M. S. Leite, *J. Phys. Chem. Lett.*, 2018, **9**, 3463–3469.
85 H. Schmidt-Böcking, K. Reich, A. Templeton, W. Trageser and V. Vill, in *Otto Sterns Veröffentlichungen – Band 2: Sterns Veröffentlichungen von 1916 bis 1926*, ed. H. Schmidt-Böcking, K. Reich, A. Templeton, W. Trageser and V. Vill, Springer Berlin Heidelberg, Berlin, Heidelberg, 2016, pp. 79–85, DOI: 10.1007/978-3-662-46962-0_5.
86 J. N. Demas, B. A. DeGraff and W. Xu, *Anal. Chem.*, 1995, **67**, 1377–1380.
87 Z. Song, J. Zhao and Q. Liu, *Inorg. Chem. Front.*, 2019, **6**, 2969–3011.
88 Y. Tian, M. Peter, E. Unger, M. Abdellah, K. Zheng, T. Pullerits, A. Yartsev, V. Sundström and I. G. Scheblykin, *Phys. Chem. Chem. Phys.*, 2015, **17**, 24978–24987.
89 F. Tian, W. Feng, B. Xing, X. He, W. A. Saidi and L. Zhang, *Adv. Energy Sustainability Res.*, 2021, **2**, 2100087.
90 M. Abdi-Jalebi, Z. Andaji-Garmaroudi, A. J. Pearson, G. Divitini, S. Cacovich, B. Philippe, H. Rensmo, C. Ducati, R. H. Friend and S. D. Stranks, *ACS Energy Lett.*, 2018, **3**, 2671–2678.
91 D. H. Chun, S. Kim, S. U. Chai, W. Kim, W. Kim, J. H. Lee, R. Rhee, D. Choi, J. K. Kim, H. Shin and J. H. Park, *Nano Lett.*, 2019, **19**, 6498–6505.
92 Y. Ding, Y. Wu, X. Feng, H. Li, E. Feng, J. Chang, C. Long, Y. Gao and J. Yang, *Commun. Mater.*, 2024, **5**, 279.
93 L. Zhao, P. Tang, D. Luo, M. I. Dar, F. T. Eickemeyer, N. Arora, Q. Hu, J. Luo, Y. Liu, S. M. Zakeeruddin, A. Hagfeldt, J. Arbiol, W. Huang, Q. Gong, T. P. Russell, R. H. Friend, M. Grätzel and R. Zhu, *Sci. Adv.*, 2022, **8**, eabo3733.

94 S. Lee, J. H. Park, B. R. Lee, E. D. Jung, J. C. Yu, D. Di Nuzzo, R. H. Friend and M. H. Song, *J. Phys. Chem. Lett.*, 2017, **8**, 1784–1792.
95 M. Abdi-Jalebi, M. I. Dar, A. Sadhanala, S. P. Senanayak, M. Franckevičius, N. Arora, Y. Hu, M. K. Nazeeruddin, S. M. Zakeeruddin, M. Grätzel and R. H. Friend, *Adv. Energy Mater.*, 2016, **6**, 1502472.
96 Y.-W. Choi, Y.-S. Jeon, D.-N. Lee and N.-G. Park, *ACS Energy Lett.*, 2024, **9**, 3754–3765.
97 W.-T. Wang, P. Holzhey, N. Zhou, Q. Zhang, S. Zhou, E. A. Duijnstee, K. J. Rietwyk, J.-Y. Lin, Y. Mu, Y. Zhang, U. Bach, C.-G. Wu, H. L. Yip, H. J. Snaith and S.-P. Feng, *Nature*, 2024, **632**, 294–300.